communications biology

A Nature Portfolio journal

Article

https://doi.org/10.1038/s42003-026-09543-9

Epigenetic and metabolic rewiring in metastatic pheochromocytomas and paragangliomas driven by *SDHB* mutations

Check for updates

Tamara Cubiella[1,2,14], Juan José Alba-Linares[1,2,3,4,14], Jaime San-Juan-Guardado[1,2], Alvaro Suarez-Priede[1,2], Nerea Gómez-Suárez[1,2], Maria Tous[5], Irina Bancos[6], Carles Villabona[7], Teresa Serrano[8], Isabel Tena[9], Maribel Del Olmo[10], Lluis Forga[11], Nuria Valdés[12], Mario F. Fraga[1,2,3,4,13] & María-Dolores Chiara[1,2]

Pheochromocytomas and paragangliomas (PPGLs) with *SDHB* mutations frequently develop metastases, but the molecular mechanisms driving this progression remain unclear. Here we show that *SDHB*-mutant metastatic PPGLs display an amplified hypermethylation signature, particularly in genes involved in neuronal differentiation, building on previous findings in *SDHx*-mutated tumors. This epigenetic shift is already detectable in benign *SDHB*-mutant tumors, suggesting early priming toward a less differentiated state. In parallel, we identify hypomethylation of genes linked to carbohydrate metabolism, notably the fructose transporter *SLC2A5*. Functional assays reveal that *SDHB* loss, hypoxia, exogenous succinate, and fructose availability promote tumor cell growth and induce cell-type–restricted, *SDHB*-dependent, induction of *SLC2A5* expression. These findings highlight the dual role of *SDHB* mutations in driving epigenetic reprogramming and metabolic adaptation, promoting tumor cell plasticity and survival under metabolic stress. By uncovering a fructose-driven metabolic vulnerability, our study provides insights into the molecular mechanisms underlying metastatic PPGLs and identifies potential therapeutic targets at the intersection of epigenetic and metabolic regulation.

Paragangliomas and pheochromocytomas (PPGLs) are a heterogeneous group of neuroendocrine tumors arising from chromaffin cells of the sympathetic and parasympathetic nervous systems. These tumors are predominantly slow-growing and typically non-aggressive, often managed through surgical resection. However, approximately 20% of PPGLs develop metastatic lesions, significantly increasing patient morbidity and mortality[1].

Genetic alterations play a crucial role in PPGL pathogenesis, particularly mutations affecting the succinate dehydrogenase (SDH) complex[2–5]. As a key component of the Krebs cycle and electron transport chain, SDH catalyzes the conversion of succinate to fumarate, preventing succinate accumulation. However, germline mutations in *SDHB*, *SDHD*, *SDHA*, or *SDHC* (collectively *SDHx*) disrupt this process, leading to oncometabolite accumulation that drives epigenetic reprogramming[6,7] and activation of hypoxia-inducible factor (HIF) target genes[8–10].

The epigenetic dysregulation is believed to play a key role in the aggressive behavior of PPGLs. Specifically, several studies have underscored the marked hypermethylation phenotype observed in PPGLs with *SDHx* mutations[11–13]. However, among this spectrum of genetic aberrations, a noteworthy distinction emerges; individuals harboring mutations in the *SDHB* gene exhibit a distinct propensity towards metastatic dissemination[14]. Therefore, the loss of SDHB function, unlike other SDH complex components, promotes epithelial–mesenchymal transition, shifting neuroendocrine cells from a differentiated, non-invasive phenotype to an undifferentiated, invasive phenotype[15]. This distinct behavior has garnered significant interest, prompting investigations into the mechanisms underlying *SDHB*-driven tumor aggressiveness[16–19].

Despite advances in PPGL research, studies specifically addressing the intersection of *SDHB* mutations and metastatic progression remain scarce[6,16,20]. This knowledge gap limits our ability to fully understand the molecular underpinnings of *SDHB*-mutant metastatic PPGLs and develop effective therapeutic strategies.

A full list of affiliations appears at the end of the paper. e-mail: mdchiara.uo@uniovi.es

In this study, we bridge this critical gap by analyzing a large cohort of metastatic PPGL cases harboring *SDHB* mutations, integrating clinical and epigenetic data to define the unique molecular landscape of these tumors. By delineating the distinct epigenetic signatures and metabolic adaptations associated with *SDHB*-mutant metastatic PPGLs, we aim to provide insights into disease progression and identify potential therapeutic vulnerabilities that could inform personalized treatment strategies for this high-risk patient population.

Results

Patients

To identify epigenomic alterations associated with malignancy in PPGL, we analyzed the DNA methylation status of 754,581 CpG sites in primary PPGL tumors using the EPICv1 microarray platform. This technology offers enhanced genome-wide coverage, providing a more comprehensive view of epigenetic dysregulation in PPGLs compared to previous studies[16,20].

Our cohort comprised 34 PPGL cases, including 20 metastatic (MT) and 14 non-metastatic (BN) tumors (Fig. 1a). Detailed clinical, genetic, and epidemiological data, along with tumor primary site information, are summarized in Table 1.

Global methylation profiling and identification of differentially methylated regions in benign and metastatic PPGLs

To explore global methylation patterns in PPGLs, we performed t-Distributed Stochastic Neighbor Embedding (t-SNE) using the beta values from the 50,000 most variable probes (Fig. 1b). This analysis revealed a clear segregation of samples into two distinct clusters: one predominantly composed of MT tumors, and the other enriched with BN tumors.

Next, we examined the distribution of beta values (Fig. 1c), which revealed a subtle but consistent increase in global methylation levels in MT compared to BN tumors ($\bar{\beta}_{MT} = 0.55$; $\bar{\beta}_{BN} = 0.53$; Wilcoxon-test $P < 0.001$). To further explore methylation differences, we identified differentially methylated positions (DMPs) between MT-PPGLs and BN-PPGLs using empirical Bayes moderated t tests (FDR < 0.05, $|\Delta\beta| > 0.10$, see Methods). This analysis yielded 4936 DMPs (Fig. 1d), of which 3994 were hypermethylated (hyper-DMPs), and 942 were hypomethylated (hypo-DMPs). The distribution and genomic localization of these DMPs are shown in Fig. 1e, f. Notably, hypermethylated DMPs were significantly enriched in CpG islands (Fisher's test $P < 0.001$, OR = 3.16), promoters ($P < 0.001$, OR = 1.45), and first exons ($P < 0.001$, OR = 1.42). In contrast, hypomethylated DMPs were primarily located in open-sea regions ($P < 0.001$, OR = 3.79) and intergenic areas ($P < 0.001$, OR = 2.30).

To identify spatially coordinated DNA methylation alterations that may drive metastatic progression, we conducted a comprehensive bioinformatics analysis to identify differentially methylated regions (DMRs) (FDR < 0.05; $|\Delta\beta| > 0.10$; see "Methods"). This analysis uncovered 935 DMRs (Supplementary Data 1), of which 883 (94%) exhibited hypermethylation, affecting 647 unique genes (Fig. 2a). Among these, 621 genes (96%) displayed hypermethylation, reinforcing the role of epigenetic silencing in metastatic transformation.

Functional enrichment analysis of the hypermethylated promoters and transcription start sites highlighted pathways related to homophilic cell–cell adhesion and tissue morphogenesis (Fig. 2b). Within this group, *PCDHGC3* (chromosomal locus 5q31), encoding a protocadherin involved in cell adhesion, emerged as the most affected locus in agreement with our previous research[21], which identified promoter hypermethylation of *PCDHGC3* as a hallmark of MT- PPGLs carrying *SDHB* mutations. A detailed analysis of a 2995 bp DMR encompassing its promoter and first exon (Fig. 2c) revealed higher methylation levels in MT-PPGLs compared to BN-PPGLs. Notably, hypermethylation was more pronounced in *SDHB*-mutated (MUT) PPGLs, both BN and MT, compared to wild-type (WT) PPGLs. This suggests a stepwise epigenetic process in which SDHB loss primes the locus for hypermethylation, which becomes further intensified during metastatic progression, consistent with methylation dynamics described for other cancer-driver genes[22,23]. In contrast, *SATB2*, a transcription factor involved in chromatin organization and developmental

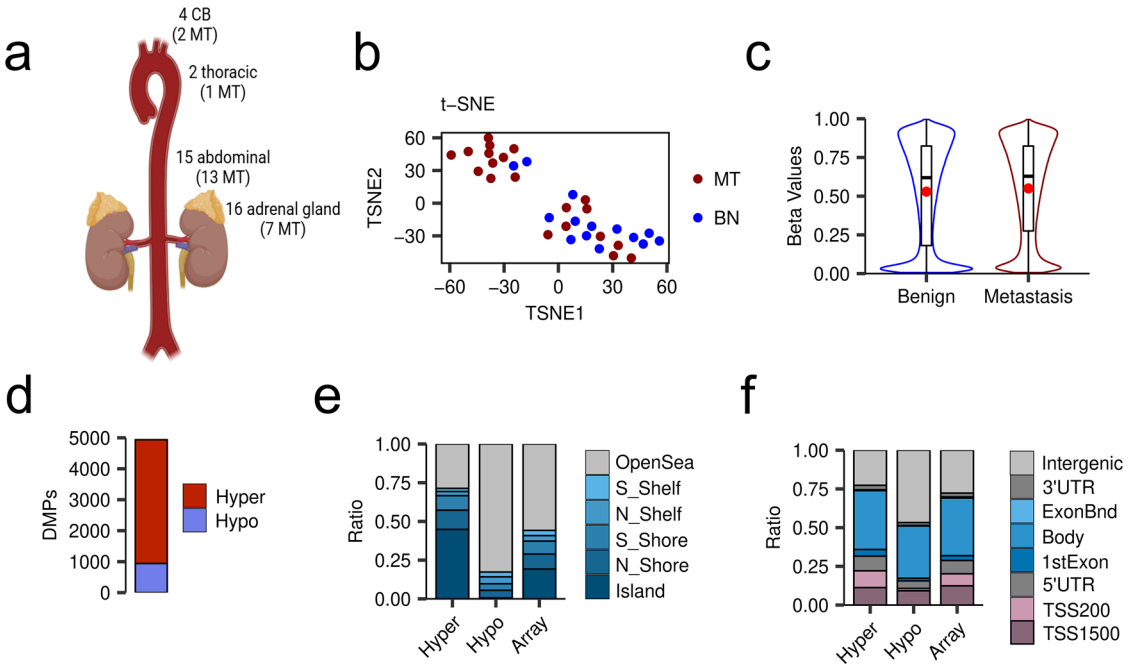

Fig. 1 | Global DNA methylation profiling reveals distinct epigenetic patterns in metastatic versus benign PPGLs. a Schematic representation of the sample cohort. CB carotid body, MT metastatic tumor. Created with BioRender.com. **b** Scatter plot displaying the tSNE projection of the samples based on methylation levels at the 50,000 most variable probes. MT metastatic, BN benign/non-metastatic. **c** Violin plots illustrating the global distribution of average beta methylation values in benign and metastatic PPGLs. **d** Bar plots showing the number of hypermethylated and hypomethylated positions (DMPs; FDR < 0.05) between MT-PPGLs and BN-PPGLs. **e**, **f** Bar plots depicting the overall distribution (**e**) and genomic localization (**f**) of hyper- and hypomethylated DMPs in MT-PPGLs versus and BN-PPGLs. The background distribution of the 754,581 analyzed probes is shown for comparison.

Table 1 | Clinical and genetic data of patients

Gender (M/F)	Age (years)	Tumor location	*SDHx* gene mutated	Gene mutation	Benign(BN) Metastatic(MT)	MT location
F	67	cervical mass	*SDHB*	c.166_170delCCTCA, pPro56fs (X5)	MT	LN
F	43	retroperitoneum	*SDHB*	deletion ex 6-8	MT	LN, bone
F	51	abdominal	*SDHB*	c.637dupA, p.Met213Asnfs*9	MT	LN
F	45	mesocolon	*SDHB*	c.1-?_72 + ?del	MT	Uterus
M	18	retroperitoneum	*SDHB*	c.637dupA, p.Met213Asnfs*9	BN	
M	36	carotid body	*SDHB*	c.(?_-151)_(72 + 1_73-1)del	BN	
F	49	para-aortic	*SDHB*	Confirmed mutation [#]	MT	LN
M	57	colon, mesentery	*SDHB*	Confirmed mutation [#]	MT	Bone, colon
M	48	cervical mass	*SDHB*	deletion ex 1	MT	Bone
F	63	adrenal gland	*SDHB*	deletion ex 6–8	MT	Hilar mass
M	64	mediastinum	*SDHB*	Confirmed mutation [#]	MT	Bone
M	14	adrenal gland	*SDHB*	deletion ex 1	BN	
M	16	retroperitoneum	*SDHB*	deletion ex 1	BN	
F	20	periaortic	*SDHB*	Confirmed mutation [#]	MT	Bone
M	22	retroperitoneum	*SDHB*	c.166_170delCCTCA; p.Pro56Tyrdelfs*5	MT	LN
F	39	adrenal gland	none		MT	Unknow
M	75	adrenal gland	none		MT	Bone
F	44	carotid body	none		BN	
F	15	adrenal gland	none		MT	LN
F	45	mesocolon	*SDHB*	c.1-?_72 + ?del	MT	Uterus and appendages
F	42	adrenal gland	none		MT	Abdominal wall, diaphragm
M	66	adrenal gland	none		MT	Liver, bone
F	77	adrenal gland	none		BN	
M	66	retroperitoneum	*SDHB*	deletion ex 1	MT	Bone
M	48	adrenal gland	none		BN	
M	69	adrenal gland	none	unknown	BN	
F	unknown	adrenal gland	*SDHB*	deletion ex 1	MT	LN
F	44	adrenal gland	none		BN	
F	61	adrenal gland	none		BN	
F	41	mediastinum	none		BN	
M	54	brain	none		MT	Bone
M	49	adrenal gland	unknown		BN	
F	39	adrenal gland	none		BN	
M	77	adrenal gland	none		BN	

[#]Details unavailable. *M* male, *F* female, *LN* lymph node.

regulation, exhibited hypermethylation only in MT tumors, irrespective of *SDHB* mutational status (Fig. 2c), indicating a distinct metastasis-specific epigenetic event.

Epigenetic deregulations associated with metastasis according to the presence or not of *SDHB* mutations

We were next interested to investigate the DNA methylation alterations ascribable to the metastatic process in MUT and WT PPGLs. Consistent with our findings when comparing MT and BN samples, we found that PPGLs with the presence or absence of mutations in *SDHB* have a similar beta methylation distribution, with a subtle increase in mean methylation value for MUT PPGLs (0.56) versus WT PPGLs (0.53) (Fig. 3a). Additionally, we identified a higher number of hyper-DMPs (25,523) compared to hypo-DMPs (3305) in MUT PPGLs versus WT PPGLs (Fig. 3b). Most hyper-DMPs were located in CpG islands (Fisher's test $P < 0.001$, OR = 1.45), genes (Fisher's test $P < 0.001$, OR = 1.26) and TSS1500 regions (Fisher's test $P < 0.001$, OR = 1.28), while hypo-DMPs were mostly found in open-sea (Fisher's test $P < 0.001$, OR = 3.38) and intergenic regions (Fisher's test $P < 0.001$, OR = 1.45) (Fig. 3c, d).

Mutations in *SDHx* genes induce a hypermethylated phenotype[6], while epigenetic deregulations are known to play a crucial role in the metastatic transformation of primary tumors[22]. Consequently, it is hypothesized that these two conditions may intersect. However, the extent of their interconnection has not been thoroughly explored. To investigate whether specific epigenetic deregulations are uniquely associated with metastasis or with SDHB dysfunction, we conducted comprehensive bioinformatic analyses.

First, we performed a comparative analysis of the DMPs found in MT versus BN tumors and those identified in MUT as compared with WT PPGLs. This analysis revealed a limited overlap between the two gene sets.

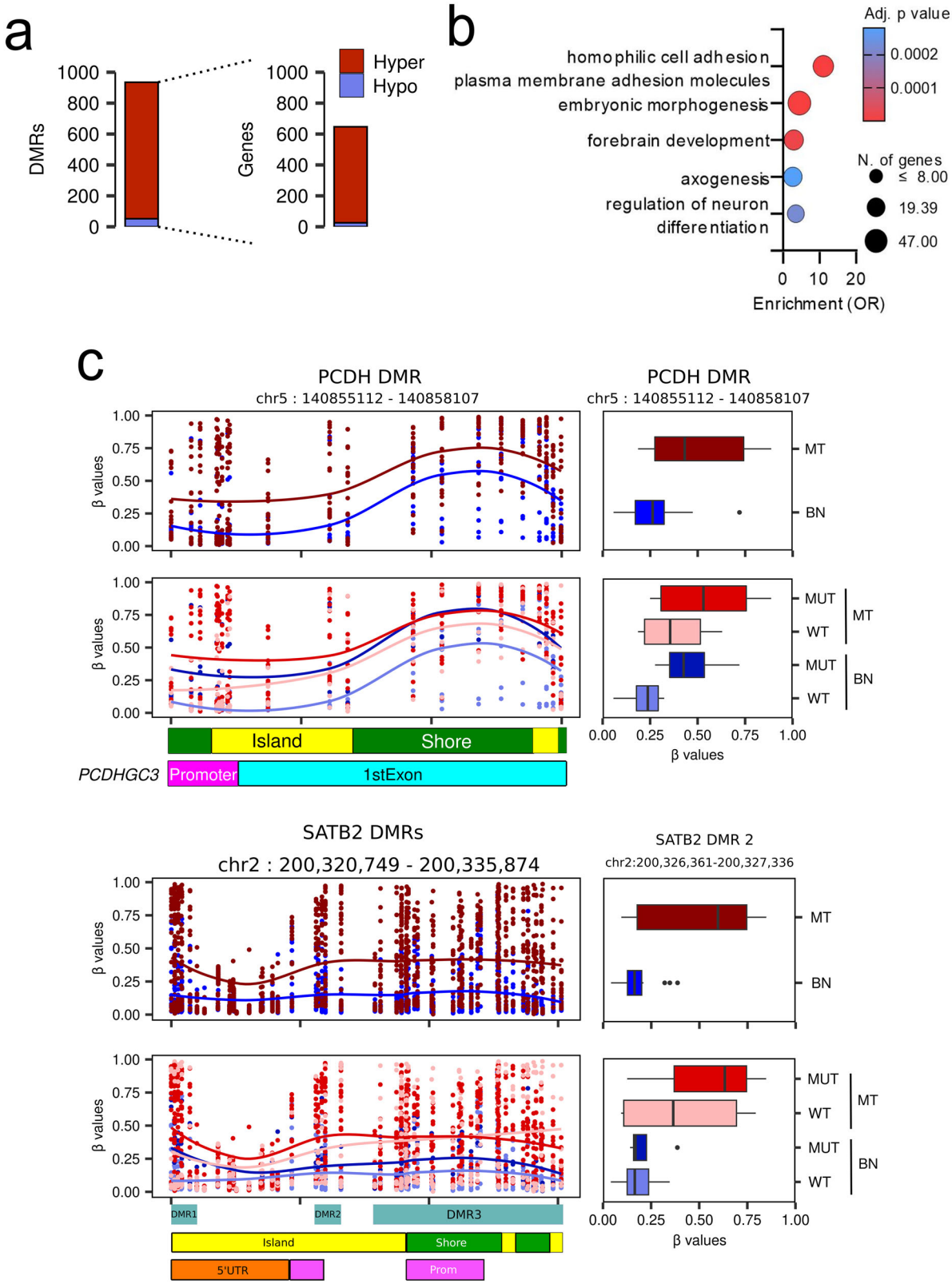

Fig. 2 | Hypermethylation of *PCDHGC3* AND *SATB2* promoter and first exon is associated with *SDHB* mutation and metastatic progression in PPGLs. a Bar plot showing the number of differentially methylated regions (DMR; FDR < 0.05) identified in MT-PPGLs versus BN-PPGLs, along with the corresponding number of affected genes. **b** Functional enrichment analysis of genes with hypermethylated promoters and transcription start sites in MT-PPGLs. **c** Left panels: Scatter plots of β values across the DMR of the *PCDHGC3* (top) and *STAB2* (bottom) genes, including smoothed trend lines by group (MT in red, BN in blue). For each gene, the top plot compares MT and BN tumors, and the bottom plot further separates samples by *SDHB* mutation status (MUT = *SDHB*-mutant, WT = wild-type). Right panels: Box plots showing average β values across the DMR for the same comparisons. Genomic context of the DMR, showing overlap with a CpG island, shore region, promoter, and first exon of *PCDHGC3* (top) and *SATB2* (bottom) is shown in the bottom scheme.

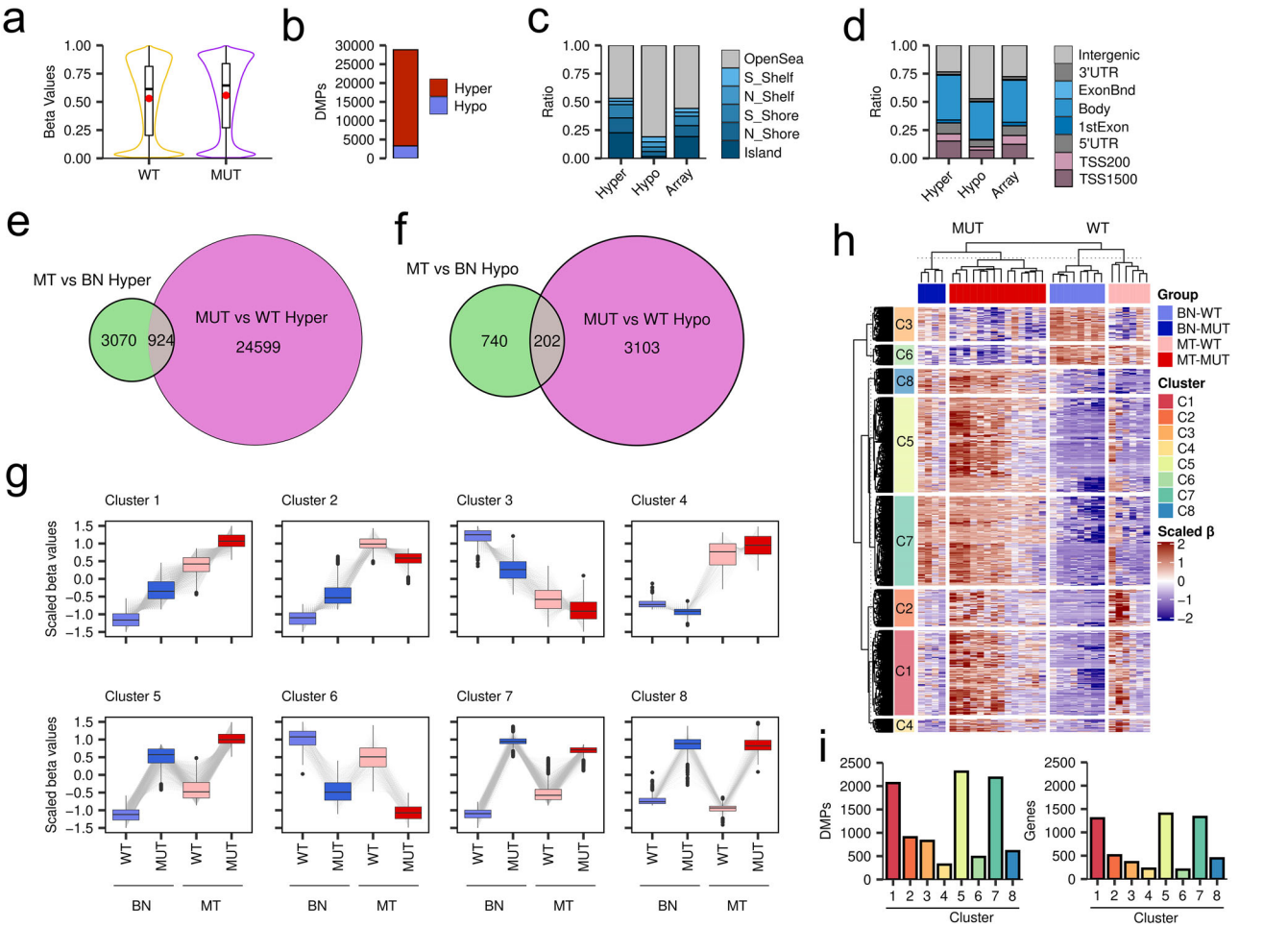

Fig. 3 | Integrative methylation analysis reveals shared and distinct epigenetic alterations in metastatic and *SDHB*-mutant PPGLs. a Violin plots showing the distribution of global methylation (β values) in wild-type (WT) and *SDHB*-mutant (MUT) PPGLs. **b** Bar plot depicting the number of hypermethylated and hypomethylated differentially methylated positions (DMPs; FDR < 0.05) in MUT versus WT PPGLs. **c**, **d** Distribution across CpG island context (**c**) and gene regions (**d**) of DMPs between MUT and WT PPGLs. **e**, **f** Venn diagrams showing the overlap of hypermethylated (**e**) and hypomethylated (**f**) DMPs between metastatic (MT) versus benign/non metastatic (BN) and MUT versus WT comparisons. **g** Scaled β values of representative DMPs grouped into eight clusters based on their methylation patterns across BN/MT and WT/MUT groups. **h** Heatmap showing hierarchical clustering of the DMPs (FDR < 0.05) across PPGL samples. Samples are grouped according to clinical status. Colors represent scaled β-values (red = hypermethylated; blue = hypomethylated). The eight methylation clusters (C1–C8) are highlighted on the left. **i** Bar plots showing the number of DMPs (left) and associated genes (right) within each cluster.

Specifically, 924 out of 3994 hyper-DMPs (23%) and 202 out of 942 hypo-DMPs (21%) identified in MT-PPGLs were also present in MUT + MT PPGLs (Fig. 3e, f). Accordingly, the majority of DMPs detected in MT tumors were not shared with those associated with *SDHB* mutation (77% of hyper-DMPs, 3070 out of 3994; and 78% of hypo-DMPs, 740 out of 942). Although this overlap initially appeared significant, permutation- and bootstrap-based analyses (see Methods) confirmed that it did not exceed random expectations once the correlation between metastasis and *SDHB* mutation status was considered ($p \gg 0.05$). These findings suggest that simple overlap analyses are insufficient to disentangle epigenetic changes driven by the metastatic process from those associated with *SDHB* mutations.

To refine our search and to identify potential epigenetic alterations specifically linked to either metastasis or SDHB loss, we performed a clustering analysis using 9872 DMPs. This dataset included all DMPs identified in the MT versus BN comparison (4936) and the 4936 most significant DMPs detected in the MUT versus WT PPGLs. This analysis identified eight distinct clusters based on variations in beta values during tumor stage transitions (Supplementary Data 2; Fig. 3g–i).

Clusters 1 and 3 included hyper-DMP and hypo-DMPs, respectively, which were present in MT-PPGLs and appeared further amplified in MUT PPGLs. This pattern suggests that SDHB dysfunction and metastasis-associated epigenetic alterations may exert additive or synergistic effects, although the effect of metastasis appears to be more pronounced than that of the mutation. Nevertheless, given the strong correlation between *SDHB* mutation status and metastatic disease in our cohort, these observations should not be interpreted as evidence of causality or temporal sequence.

Among the clusters enriched in hyper-DMPs, distinct profiles were observed. Cluster 4 included loci specifically hypermethylated in MT tumors, independent of *SDHB* mutation, indicating a metastasis-driven effect. In contrast, cluster 8 showed hypermethylation restricted to MUT PPGLs, regardless of whether the tumor was BN or MT, suggesting that these changes are primarily attributable to loss of *SDHB* function. Clusters 5 and 7 shared similar methylation dynamics with cluster 8. Cluster 5 contained CpGs where *SDHB* mutation and metastasis both contributed to hypermethylation, but the effect of *SDHB* mutation was stronger, indicating that *SDHB* loss exerts a dominant influence over tumor behavior in these regions. In cluster 7, *SDHB* mutation alone drove methylation to maximal levels, with no further increase associated with metastasis, suggesting that this signature is primarily *SDHB*-dependent and metastasis-independent.

Cluster 6 contained hypo-DMPs that appeared unrelated to tumor status (BN or MT). Unlike hyper-DMPs, no hypo-DMPs were specifically

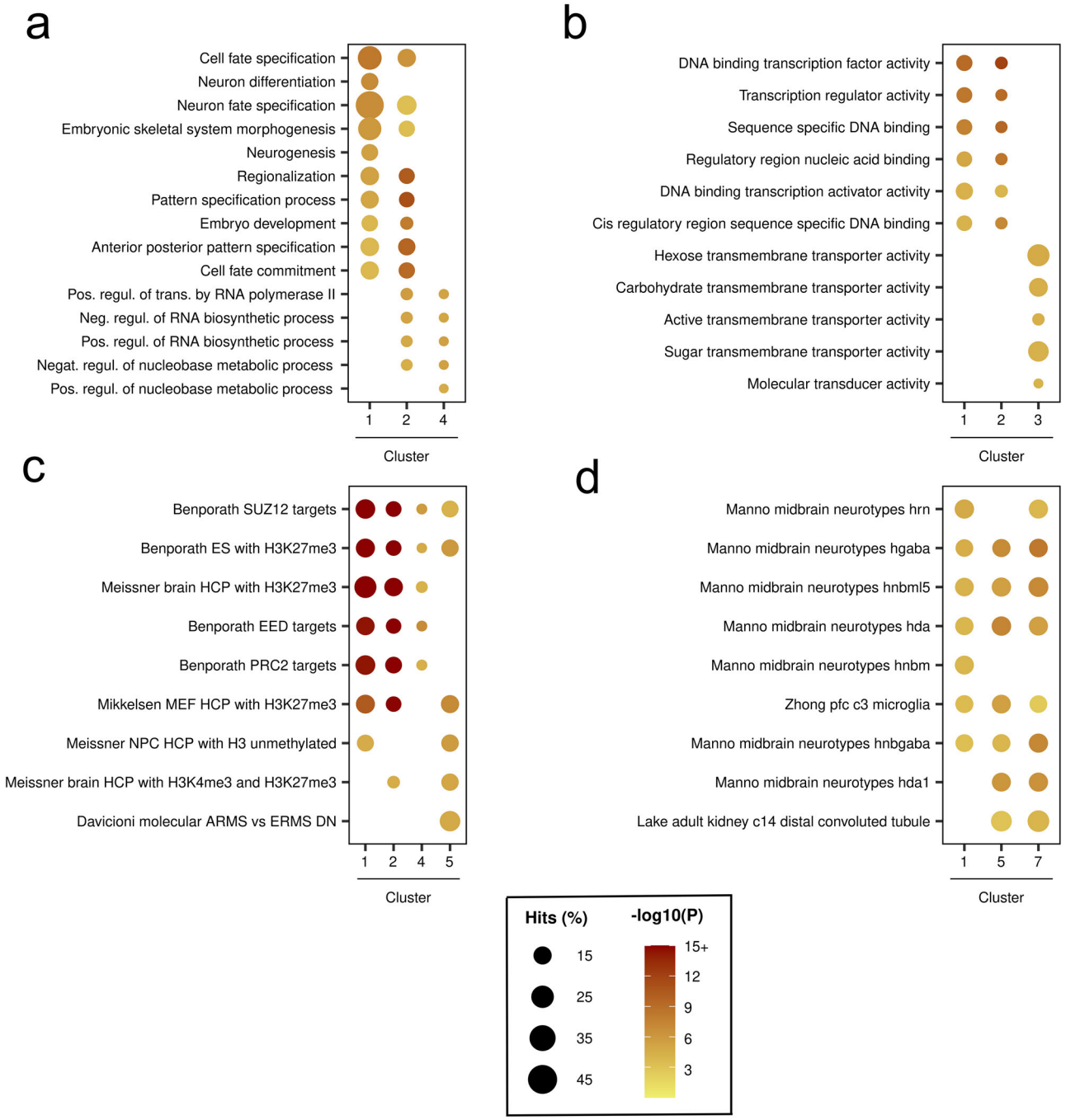

Fig. 4 | Functional enrichment analysis reveals cluster-specific biological processes and epigenetic signatures associated with differentially methylated regions in metastatic and *SDHB*-mutant PPGLs. Bubble plots showing the top 5 most significant gene ontology (GO) biological processes (**a**), GO molecular functions (**b**), chemical and genetic perturbation gene sets (**c**), and cell-type–specific gene expression signatures (**d**) for the indicated clusters.

associated with metastasis irrespective of *SDHB* status. Finally, cluster 2 exhibited an intermediate methylation profile between clusters 1 and 4.

Functional implications of cluster-specific methylation changes: neuronal differentiation and carbohydrate transport in metastatic PPGLs

To unravel the potential functional significance of the identified methylation changes, gene ontology analysis was performed for DMPs within each cluster (Fig. 4). Clusters 1 and 2 were strongly enriched for targets of the PRC2/EED–EZH2 polycomb complex, including embryonic stem-cell gene sets and neural lineage differentiation programs. Several of these genes were also present in cluster 4 (e.g., *EMX1, HOXB3, LHX4, MSX1, ZMIZ1*). However, cluster 4 displayed a distinct signature with a stronger enrichment in transcription factors that control neuronal identity and cell-fate specification (*POU4F1, SIM2, ZIC1, SMARCD3, TCF4, ZFHX3, PRRX2, HHEX, SOX15, TBX5, EBF2, EVX2, PAX3, PAX5, PITX1, PITX2, MECOM, HOXC13* and *NKX-1.2*). Clusters 1, 2, 5, and 7 contain the largest number of hypermethylated CpG sites associated with metastatic status and/or *SDHB* mutation and converge on similar neuronal lineage programs. These overlapping enrichments indicate that *SDHB* loss and metastatic progression converge on a shared epigenetic trajectory, centered on repression of neuronal differentiation and lineage-identity regulators.

The comparison of clusters 1, 2, and 3 was designed to contrast hypermethylated (clusters 1 and 2) versus hypomethylated (cluster 3) loci.

As expected, hyper- and hypomethylation mapped to distinct functional programs. Notably, the hypo-DMPs in cluster 3 were significantly enriched in genes involved in carbohydrate transmembrane transport. These include *TMEM144* and *MFSD4A*, associated with glucose transport; *SLC2A5*, a well-known fructose transporter; *SLC5A10*, involved in mannose and fructose transport; *SLC2A9*, which transports both glucose and fructose; and *SLC5A2*, primarily a glucose transporter. Key metabolic regulators such as *NR5A2*, a nuclear receptor that modulates lipid and glucose metabolism, and *LDHA*, a canonical HIF1α-glycolytic target, also exhibited hypomethylation within this cluster. The identification of hypo-DMPs in genes involved in carbohydrate transmembrane transport suggests epigenetic deregulation that may facilitate enhanced nutrient uptake. This is consistent with the well-established metabolic shift in *SDHB*-mutated PPGLs toward increased glycolysis and reduced oxidative phosphorylation.

Hypomethylation in metastatic/*SDHB*-mutated tumors aligns with hypoxia-driven transcription

To assess potential transcriptional consequences of hypomethylation, we first analyzed RNA-seq data previously generated in rat pheochromocytoma PC12 cells exposed to hypoxia for 12, 24, and 48 h[24]. Although PC12 cells under hypoxia do not fully recapitulate *SDHB* loss, hypoxia is a well-established downstream consequence of SDH deficiency due to sustained HIF stabilization. Thus, this dataset provided a relevant surrogate to interrogate transcriptional programs associated with a pseudohypoxic state.

Among the genes identified within hypomethylated cluster 3, the fructose transporter *SLC2A5* displayed a significant, time-dependent upregulation under hypoxia. Other carbohydrate transporters exhibited heterogeneous responses (Supplementary Fig. S2): *SLC2A9* was upregulated after 24 h of hypoxia, *MFSD4A* showed a significant increase at 48 h but not at an earlier time point. In contrast, *SLC5A10* expression remained unchanged across all time points. As expected, *LDHA* was robustly upregulated, consistent with hypoxia-driven activation of glycolysis. Together, these data indicate that while several carbohydrate transporters respond variably to hypoxia, *SLC2A5* consistently exhibits transcriptional activation, positioning it as a candidate mediator of metabolic adaptation. *SLC2A5* encodes the fructose transporter GLUT5, which mediates fructose uptake, a process increasingly recognized as a key metabolic pathway supporting tumor initiation and progression[25].

In the context of *SDHB*-mutant PPGLs, this finding is particularly relevant. These tumors exhibit high glycolytic activity and poor vascularization, leading to local glucose depletion despite normal or elevated systemic glucose levels[26]. Because fructose metabolism bypasses key regulatory glycolytic checkpoints, we hypothesized that PPGL cells may exploit fructose uptake as an alternative carbon source to sustain proliferation under glucose limitation and pseudohypoxia. To test this hypothesis experimentally, cellular models capable of reflecting PPGL biology were required.

Due to the absence of established PPGL cell lines, we generated three patient-derived PPGL models: PGLa (from an *SDHx*-wild-type vagal paraganglioma), PCC (from an *SDHx*-wild-type pheochromocytoma), and PGLb (from an *SDHD*-mutant carotid body paraganglioma). PGLa and PCC cells were initially cultured in suspension to promote spheroid formation, thereby preserving their native neuroendocrine cytoarchitecture, and subsequently dispersed and plated under adherent conditions for phenotypic and transcriptomic analyses (Fig. 5a). In contrast, PGLb failed to form spheroids and were therefore maintained exclusively as a 2D adherent monolayer, suggesting intrinsic differences in cell–cell or cell–matrix interactions associated with the *SDHD*-mutant state.

All models retained key chromaffin features, as evidenced by tyrosine hydroxylase and nestin expression (Fig. 5b). Synaptophysin staining showed the expected punctate cytoplasmic pattern characteristic of secretory granules with additional nuclear signal of uncertain functional relevance (Fig. 5b). Notably, all models displayed nuclear accumulation of HIF2α (Fig. 5c), consistent with the stabilization pattern observed in PPGL tumors[27]. These cultures exhibited low proliferative capacity, consistent with the slow-growing nature of their tumors of origin (Fig. 5d).

Fructose supports proliferation in PPGL patient-derived cultures under hypoxia and pseudohypoxia

Glucose depletion markedly impaired proliferation in all PPGL-derived cell lines, with growth almost abolished in PGLa and reduced by 32% in PCC (Fig. 6a). Under glucose-deprived conditions, fructose supplementation significantly restored proliferation in PGLb and PCC cells (Fig. 6b), indicating that fructose can serve as an alternative metabolic fuel for PPGL cells. Given that hypoxia is a key selective pressure in *SDHB*-mutant metastatic PPGLs[26,28], we next evaluated cell proliferation under hypoxic conditions. Hypoxia significantly increased proliferation in the three models, and fructose supplementation further enhanced this effect, revealing a synergistic interaction between hypoxia and fructose availability in supporting cell viability under metabolic stress.

To validate the involvement of the fructose transporter GLUT5, we assessed *SLC2A5* expression in our PPGL-derived cell lines and compared it with unrelated tumor cell lines, HeLa and MCF7. *SLC2A5* expression was markedly higher in PPGL cells than in HeLa and MCF7 cells (>10-fold, $p < 0.0001$; Fig. 6c).

Because *SDHB*-mutant PPGLs accumulate succinate, which inhibits prolyl hydroxylases and stabilizes HIFs (pseudohypoxia), we next assessed whether *SLC2A5* is responsive to HIF-activating stimuli. Exposure of PPGL cells to hypoxia or to methyl-succinate, a membrane-permeable succinate analog that induces pseudohypoxia by inhibiting prolyl hydroxylases, significantly increased *SLC2A5* expression (Fig. 6d, e). Importantly, neither hypoxia nor methyl-succinate induced *SLC2A5* in HeLa or MCF7 cells, indicating that this response is specific to chromaffin-derived cells.

These results align with the transcriptional activation of *SLC2A5* observed in PC12 cells under hypoxia, confirming that chromaffin-lineage cells selectively upregulate *SLC2A5* in response to hypoxia or succinate-driven pseudohypoxia.

Regulation of *SLC2A5* is highly specific and distinct from canonical glucose transporters

To investigate whether *SLC2A5* regulation is specific or part of a broader carbohydrate transporter response, we compared its expression with *SLC2A1* (GLUT1) and *SLC2A8* (GLUT8). As expected, *SLC2A1* was robustly induced by hypoxia in all cell lines, including PC12, with the strongest increase observed in HeLa cells, consistent with its role as a well-established HIF-responsive target. *SLC2A8* also increased under hypoxia, but only in HeLa and MCF7, whereas it decreased in PPGL and PC12 cells, consistent with previous reports in other models (Fig. 6f, g)[29,30]. When cells were exposed to extracellular succinate, *SLC2A1* expression decreased, and *SLC2A8* remained unchanged or variably increased depending on the PPGL model (Supplementary Fig. S3). Collectively, these data demonstrate that *SLC2A5* uniquely responds to both hypoxia and succinate-induced pseudohypoxia, distinguishing it from canonical hypoxia-responsive glucose transporters such as *SLC2A1*.

SDHB knockout induces *SLC2A5* only in models with pseudohypoxic HIF2α activation

Because *SLC2A5* induction occurred only in PPGL-derived models, characterized by constitutive or inducible HIF2α stabilization, we next assessed whether *SDHB* loss alone was sufficient to activate *SLC2A5*. Using CRISPR/Cas9, we generated *SDHB*-knockout (*SDHB*-KO) HeLa and MCF7 cells. In parallel, we analyzed the *SDHB*-KO renal carcinoma cell line 786-O, previously generated in our laboratory[21], which lacks functional VHL and consequently exhibits constitutive HIF2α stabilization, recapitulating the pseudohypoxic state of *SDHB*-mutant PPGLs. Efficient SDHB loss at both the mRNA and protein levels was confirmed in all models (Fig. 6h). Strikingly, *SLC2A5* expression increased 1.84-fold in *SDHB*-KO 786-O cells and was likewise induced under hypoxia (1% O_2, 24 h treatment; Fig. 6j). In contrast, no induction occurred in *SDHB*-KO HeLa or MCF7 cells. These results show that *SDHB* loss alone is insufficient to activate *SLC2A5* in non-chromaffin tumor contexts; instead, its upregulation requires a permissive

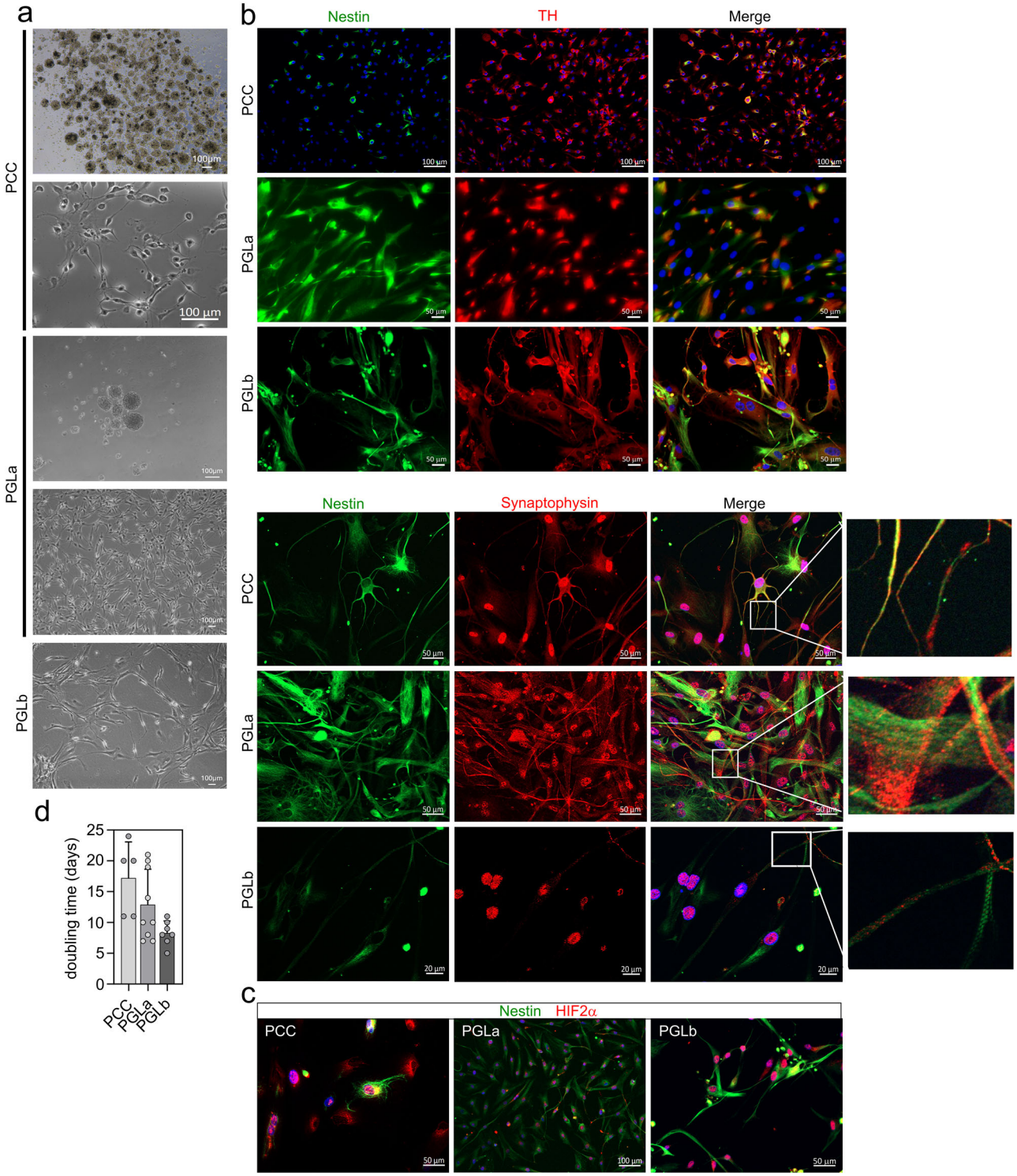

Fig. 5 | Characterization of patient-derived PPGL cell models. a Representative brightfield images showing culture morphology of the tumor-derived PPGL cell models at different stages of adaptation in vitro. PGLa (vagal paraganglioma), PCC (adrenal pheochromocytoma), and PGLb (carotid body paraganglioma). Cells were initially maintained in suspension to promote spheroid formation and subsequently plated for adherent growth prior to characterization. Scale bars, 100 µm. **b** Immunofluorescence analysis confirming preservation of key chromaffin/neuroendocrine features in the three PPGL models. Upper panels show expression of nestin (green) and tyrosine hydroxylase (TH, red); lower panels show nestin (green) and synaptophysin (red). Merged images include nuclear counterstaining (DAPI, blue). Boxed regions indicate areas shown at higher magnification to highlight punctate synaptophysin staining consistent with neurosecretory granules. **c** Immunofluorescence staining showing co-expression of nestin (green) and HIF2α (red) in PCC, PGLa, and PGLb cells, indicating retention of hypoxia-related signaling features characteristic of PPGLs. Nuclei are counterstained with DAPI (blue). **d** Quantification of the average doubling time (in days) of the three patient-derived cell lines. Cells were passaged at confluence, and doubling times were calculated based on the interval between passages over multiple consecutive passages (minimum of five passages per cell line). Bars represent mean values, and error bars indicate standard deviation, reflecting variability in proliferation rates.

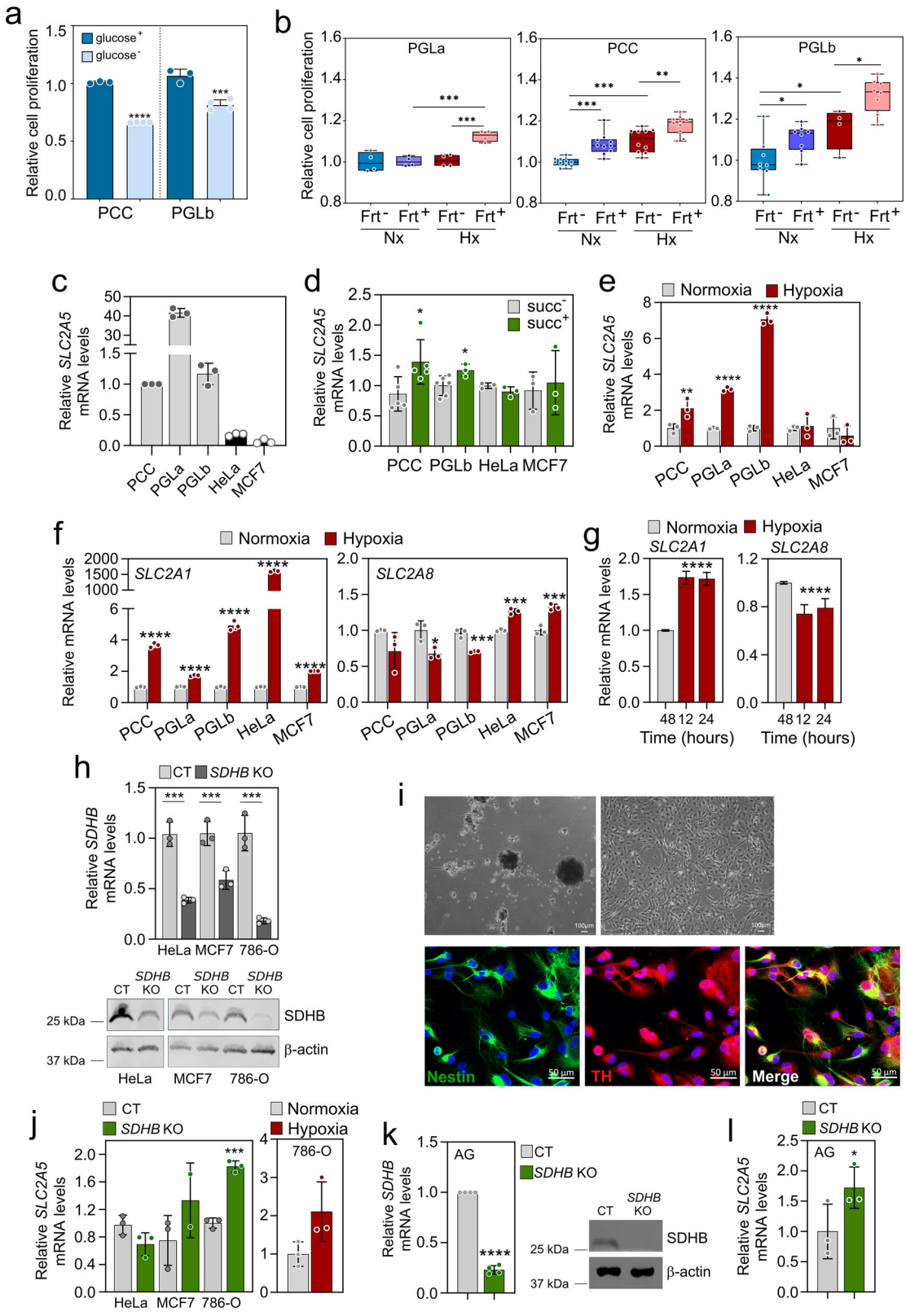

pseudohypoxic program, such as HIF2α stabilization, and/or lineage-specific neuroendocrine features.

To test whether this regulatory mechanism also operates in a non-tumoral adrenal context, we generated *SDHB* KO cells from primary human adrenal gland (AG) cells. These cells were maintained under both spheroid-forming and adherent conditions using the same protocols applied to PPGL-derived models. Like PPGL cells, AG cultures retained key chromaffin characteristics, including tyrosine hydroxylase and nestin expression (Fig. 6i), and exhibited slow proliferation rates (doubling time ~10 days). Efficient *SDHB* KO was verified at both the mRNA and protein levels (Fig. 6k). Importantly, *SDHB*-deficient AG cells also exhibited upregulation of *SLC2A5* (Fig. 6l), further demonstrating that *SDHB* loss alone is sufficient

Fig. 6 | *SLC2A5* expression is upregulated by hypoxia, succinate and *SDHB* knockout. **a** Relative proliferation of PCC and PGLb cells cultured under glucose-deprived (glucose$^-$) versus glucose-containing (17 mM, glucose$^+$) conditions. **b** Proliferation of the indicated cell lines cultured under normoxia (Nx) or hypoxia (1% O_2; Hx) in glucose-deprived conditions, with or without supplementation of 12 mM fructose (Frt$^+$/Frt$^-$). **c** Baseline *SLC2A5* mRNA levels in PPGL-derived cells (PCC, PGLα, PGLb) and cancer cell lines (HeLa, MCF7). **d** *SLC2A5* expression following treatment with 1 mM succinate (succ$^-$ versus succ$^+$) for 24 h in PPGL-derived and cancer cells. **e**, **f** mRNA levels of *SLC2A5* (**e**) and *SLC2A1*/*SLC2A8* (**f**) in the indicated cell lines cultured under normoxia or hypoxia (1% O_2, 24 h). **g** Relative mRNA levels of *SLC2A1* and *SLC2A8* in PC12 cells cultured under normoxia or hypoxia (1% O_2) for the indicated time points. **h**, **k** *SDHB* mRNA levels and protein expression in control (CT) and *SDHB* KO cells. Panel **h** shows tumor cell lines (HeLa, MCF7, 786-O); panel **k** shows non-tumoral adrenal gland (AG) cells. β-actin was used as a loading control. **i** Representative images of the AG cell model. Top: brightfield images showing spheroid formation in suspension culture (left) and subsequent adherent growth after plating in FBS-containing medium (right). Bottom: immunofluorescence staining showing nestin (green) and tyrosine hydroxylase (TH, red); nuclei are counterstained (blue). **j**, **l** *SLC2A5* expression upon *SDHB* KO. Panel **j** shows expression in tumor cell lines (HeLa, MCF7, 786-O), including 786-O cells under hypoxia (1% O_2, 24 h). Panel **l** shows expression in non-tumoral AG cells. ($n = 3$ biologically independent samples). Expression is shown relative to control (CT). All data represent the mean ± SEM of at least three independent experiments. $^*P < 0.05$, $^{**}P < 0.01$, $^{***}P < 0.001$, $^{****}P < 0.0001$.

to drive *SLC2A5* expression in neuroendocrine cells, independently of tumor-derived alterations.

Collectively, our findings identify *SLC2A5* as a downstream effector of SDHB deficiency and HIF2α stabilization, linking epigenetic–metabolic reprogramming to fructose utilization in PPGLs and other pseudohypoxic contexts. Importantly, *SLC2A5* induction is observed only in cellular settings characterized by HIF2α stabilization or neuroendocrine features, rather than arising as a generic hypoxic response.

Discussion

Our findings reveal a complex interplay between *SDHB* mutations, epigenetic dysregulation, and metabolic rewiring in PPGLs. *SDHB* mutations are known to induce a hypermethylated phenotype[6,15], supporting the hypothesis that they create a pro-tumorigenic environment by disrupting normal epigenetic regulation. Here, we show that *SDHB* mutations and metastasis affect both overlapping and distinct sets of genes, revealing that metastatic progression involves additional epigenetic changes beyond those imposed by *SDHB* loss.

Notably, both *SDHB*-mutated and metastatic tumors exhibit hypermethylation of PRC2/EED–EZH2 targets, a complex that represses differentiation and promotes stemness and lineage plasticity[31–35]. The fact that these PRC2-regulated genes are already hypermethylated in benign *SDHB*-mutated tumors suggests that *SDHB* loss may epigenetically prime chromaffin cells toward a less differentiated state even before metastatic dissemination occurs. Interestingly, several metabolic genes previously shown to be upregulated upon EZH2 inhibition[36,37] were located within our *SDHB*-associated hypermethylated clusters. This partial overlap suggests that *SDHB* loss may converge on a subset of PRC2/EZH2-regulated loci through a distinct, methylation-based mechanism.

We also extend our previous findings on the protocadherin gene *PCDHGC3*[21], demonstrating that its promoter hypermethylation is significantly higher in metastatic *SDHB*-mutated tumors than in benign *SDHB*-mutated PPGLs. This additional hypermethylation may lead to irreversible silencing of this tumor suppressor, weakening cell–cell adhesion and facilitating invasion and metastatic spread. This suggests that SDHB dysfunction and metastasis-associated epigenetic alterations may act in an additive manner, without implying causality or temporal precedence between the two processes. Disentangling the individual contributions of *SDHB* mutations and metastatic status remains challenging, largely due to the limited sample size and the strong co-occurrence of both features in our cohort. Larger, more balanced cohorts including metastatic and non-metastatic *SDHB*-mutated tumors will be required to determine whether these alterations arise sequentially or represent parallel epigenetic trajectories.

Beyond these shared patterns, metastatic tumors, independent of *SDHB* status, showed hypermethylation of transcription factors critical for chromatin organization, neurogenesis, and lineage commitment (*SATB2*, *POU4F1*, *SIM2*, *MAML3*, *NCOA2*, *PAX3*, *TCF4*, and *ZFHX3*). Unlike *PCDHGC3*, these genes were not altered in benign *SDHB*-mutated tumors, suggesting that their epigenetic change represents metastasis-specific events that contribute to tumor dedifferentiation and aggressiveness. Of note, *MAML3* gene fusions have been associated with PPGL pathogenesis and metastasis, further supporting the role of lineage transcription factors in disease progression[38].

Unexpectedly, while most epigenetic alterations associated with *SDHB* loss and metastasis involved hypermethylation, we identified a subset of hypomethylated genes enriched in extracellular carbohydrate transport. Among them, *SLC2A5*, encoding the fructose transporter GLUT5, emerged as the most prominent candidate. We found that extracellular succinate and hypoxia induce *SLC2A5* expression in PPGL-derived cell models. Consistent with our observations, *SLC2A5*/GLUT5 upregulation has been demonstrated in independent tumor models, especially in nutrient-deprived microenvironments where glucose availability is limited[39–45]. In addition, we found that other carbohydrate transporters, including *SLC2A1* (GLUT1), a canonical hypoxia–responsive gene, and *SLC2A8*, did not exhibit similar induction, supporting that this is not part of a generic hypoxic metabolic program, at least in PPGL-derived cells. Moreover, this response was absent in unrelated epithelial cancer models subjected to *SDHB* knockout or hypoxia, indicating that *SLC2A5* induction is not a universal metabolic stress response. Using primary human adrenal cells, we show that *SDHB* knockout alone is sufficient to activate *SLC2A5* in non-neoplastic adrenal cells, further supporting a cell-type-restricted and *SDHB*-dependent mechanism. Interestingly, *SLC2A5* upregulation was also observed in a renal cancer cell model that constitutively stabilizes HIF2α, like PPGL cells, suggesting that cellular contexts with high HIF2α activity may be permissive for *SLC2A5* induction.

Functionally, fructose supplementation enhanced proliferation under metabolic stress (glucose restriction and hypoxia) in PPGL-derived cells, positioning fructose as an alternative carbon source in pseudohypoxic tumors. This aligns with emerging evidence that fructose metabolism supports tumor growth and survival in nutrient-poor microenvironments[25,46–48]. Taken together, our data reveal a mechanism whereby *SDHB* deficiency promotes fructose utilization through epigenetic activation of *SLC2A5*, providing metabolic flexibility in low-oxygen, low-glucose niches of metastatic PPGLs.

In summary, we propose a model in which *SDHB* loss epigenetically primes chromaffin cells toward dedifferentiation, while metastasis imposes additional epigenetic constraints affecting lineage regulators. In parallel, *SDHB* deficiency triggers a metabolic shift involving *SLC2A5*-mediated fructose uptake, enabling tumor cells to proliferate under nutrient- and oxygen-restricted conditions. These findings establish a link between epigenetic reprogramming, metabolic plasticity, and microenvironmental stress responses and highlight *SLC2A5* as a potential metabolic vulnerability in PPGLs.

Materials and methods

Tumor samples

Tumor tissue samples were collected from 37 patients diagnosed with PPGL between 2003 and 2019. Patients were treated at the Hospital Universitario Central de Asturias (Spain), Mayo Clinic (USA), Hospital Universitario de Bellvitge (Spain), Hospital Provincial de Castellón (Spain), Hospital Universitario La Fe (Spain), and Complejo Universitario de Navarra (Spain).

Informed consent was obtained from each patient, and the study was approved by the ethical committee of the Hospital Universitario Central de Asturias. The methods were carried out in accordance with the approved guidelines and the principles expressed in the 1975 Declaration of Helsinki, as revised in 1983. All ethical regulations relevant to human research participants were followed. Clinical data were collected from patients' medical reports and are summarized in Table 1. All patients included in this study were genetically screened for germline mutations in the *SDHA*, *SDHB*, *SDHC*, and *SDHD* genes using targeted next-generation sequencing.

Genome-wide DNA methylation profiling

For paraffin-embedded (FFPE) samples, each tumor sample was reviewed by two qualified pathologists before genomic DNA extraction with the E.Z.N.A. FFPE DNA kit (Omega Bio-Tek). Quality check was performed in 2 ng of DNA using the Infinium HD FFPE QC Assay Kit (Illumina San Diego, CA, USA). Samples with a ΔCq greater than 5 were excluded. Suitable samples were bisulfite-converted using the EZ-96 DNA Methylation-Gold™ Kit (ZymoResearch, Irvine, CA, USA), starting with 300 ng of DNA and eluting the samples in 10 µl of the elution buffer supplied by the kit (M-Elution buffer). For DNA restoration, 8 µl of the bisulfite-converted samples were used, and the Infinium HD FFPE DNA Restore Kit (Illumina) was employed. Finally, the ZR-96 DNA Clean and Concentrator-5 Kit (Zymo Research) was used to clean the DNA samples, eluting them in a final volume of 10 µl of ddH_2O. DNA from frozen tissue samples was extracted using the QIAamp DNA Kit (QIAGEN, Hilden, Germany), and the EZ-96 DNA Methylation Kit (Zymo Research) was used to perform bisulfite conversion on the extracted DNA. Finally, converted DNA samples were hybridized to Infinium MethylationEPIC v1.0 BeadChip using the standard Illumina Infinium HD Methylation Assay protocol.

Methylation array data preprocessing

First, the *minfi* package (v.1.32.0)[49] was used to import fluorescence signal intensity files (IDAT) associated with each sample. The *getSex* function from the same package enabled tracking of self-reported sex based on probes targeting the X and Y chromosomes. Sample mislabeling was further assessed using SNP probe methylation patterns via the *getSnpBeta* function from *minfi*. After quality control evaluations, intensity values were background-corrected in *minfi* using the ssNoob approach[50] and subsequently, associated β-values were normalized in *ChAMP* (v.2.16.2) using the BMIQ method[51]. All samples were finally tested to follow a bimodal-shaped beta distribution profile.

Probe filtering was performed according to the following criteria: (a) detection p-value > 0.01 in any sample; (b) sex chromosome location; (c) cross-reactive or multi-mapping described activity[52], and (d) presence of SNPs with MAF ≥ 0.01 at their CpG or SBE sites (dbSNP v.147). The final number of probes that passed through all the filters was 754,581. All data analyses were performed using the statistical software R (v.4.0.2).

Single-site differential methylation analysis

Initially, M-values (which are more homoscedastic than betas[53] were obtained from the logit-transformation of normalized beta values using the *beta2m* function of the *lumi* package (v.2.40.0). Then, linear models were built to detect differentially methylated probes (DMPs) based on metastasis or *SDHB* mutational status via the *limma* package (v.3.44.3)[54]. DMPs were defined using empirical Bayes-moderated *t*-tests after adjusting for multiple testing (FDR < 0.05). In addition, DMPs were selected to have an absolute methylation difference greater than 10% ($|\Delta\beta| > 0.10$) in both paraffin and fresh samples, separately.

To assess whether the overlap between *SDHB*-associated and metastasis-associated CpGs exceeded random expectation, we applied two alternative empirical approaches[55]

(a) Permutation-based significance testing. A total of 1000 null empirical datasets were generated by multivariate normal sampling, preserving the observed correlation between log fold-change values from *SDHB* and metastasis comparisons. For each iteration, CpG overlap and odds ratio (OR) were calculated separately according to the direction of methylation change, and empirical p-values were then derived from the resulting null distributions.

(b) Bootstrapped significance testing. Differential methylation analyses were repeated 1,000 times with balanced re-sampling across the four *SDHB*-metastasis groups. Overlap significance was evaluated in each iteration using Fisher's exact test, and empirical p-values were obtained from the resulting null distributions.

Regional differential methylation analysis

Differentially methylated regions (DMRs) were detected using the "comb-p" method[56], based on the spatial distribution of *limma* p-values, as implemented in the *Enmix* package (v.1.28.2, with default parameters)[57]. DMRs were defined with an FDR < 0.05 and Sidak FDR < 0.05. In addition, DMRs with an unclear direction of methylation change were filtered out (at least 66% of their CpGs must be either hyper- or hypo-methylated), and those with average methylation differences lower than 10% in both paraffin and fresh samples.

Cluster-based classification of DNA methylation patterns according to metastasis and *SDHB* mutation status

To decipher the relationship between metastasis and *SDHB* mutation status at DNA methylation, we performed clustering analysis based on scaled, normalized average beta values of DMPs across the four groups resulting from the combination of each feature. Since the number of DMPs in metastasis was notably lower, we selected the same number of DMPs with *SDHB* mutation, prioritizing the most significant ones. Clusters were then defined using Spearman correlation distances, with the optimal number determined using the within-cluster sum of squared errors method.

Probe annotation

Each probe was annotated to its CGI (CpG Island) and gene location status using the IlluminaHumanMethylationEPICanno.ilm10b4.hg19 package (v.0.6.0). DMRs were single-annotated based on probe-level features, following this priority: (1) "Island" > "N_Shore" > "S_Shore" > "N_Shelf" > "S_Shelf" > "OpenSea"; and (2) "TSS1500" > "TSS200" > "5'UTR" > "1stExon" > "Body" > "ExonBnd" > "3'UTR" > "Intergenic". Probe annotation and intersection enrichments were assessed using Fisher's exact tests, with EPIC filtered probes as reference when needed.

Gene set enrichment analysis

DMP functionality was profiled using the *gsameth* function from the *missMethyl* package (v.1.22.0)[58], applied to gene sets from the *msigdbr* package (v.7.2.1, Molecular Signatures Database (MSigDB)[59]. Similarly, DMR functions were interrogated with the *gsaregion* function. Both methods corrected enrichment analysis results for the bias caused by the differential number of probes mapped to each gene on the array.

Cell culture

Fresh human samples of PPGLs and non-tumoral adrenal glands (AG) were obtained from patients and brain-dead organ donors undergoing multi-organ procurement surgery, respectively, at the Hospital Universitario Central de Asturias (Oviedo, Spain). The study was approved by the Research Ethics Committee on Medicinal Products of the Principality of Asturias (Code 2020.547; Oviedo, Spain) and written informed consent was obtained from all participants or, in the case of organ donors, from their next of kin prior to sample collection. Details are reported in Supplementary Table 1. Tissues were cut into 3–5 mm^3 pieces, minced, and with TrypLE™ Express (ThermoFisher, Waltham, MA, USA) and Accutase (Stemcell Technologies, Vancouver, BC, Canada) at 1:1 ratio containing 100 µM Y-27632 (MedChemExpress, Monmouth Junction, NJ, USA) and 3 mg/ml of dispase (Sigma-Aldrich, St. Louis, MO, USA) at 37°C for 45 min. The digested tissue suspension was sheared using a 1 ml pipette tip and strained over a 70 µm MACS SmartStrainer (Miltenyi Biotec, Bergisch Gladbach, Germany). The filtered tissue suspension was centrifuged at 1300 r.p.m., and

the supernatant was removed. Erythrocytes were lysed in 1 ml of red blood cell lysis buffer (ACK buffer, ThermoFisher) for 5 min at room temperature and then washed twice with 10 ml PBS. Finally, the pellet was resuspended in appropriate volume of advanced Dulbecco's Modified Eagle Medium/Ham's F-12 (DMEM/F-12, ThermoFisher) supplemented with 15% fetal bovine serum (FBS) (ThermoFisher), previously inactivated for 30 min at 56 °C; 50 ng/ml epidermal growth factor (EGF) (Stemcell Technologies); 50 ng/ml basic fibroblast growth factor (bFGF) (Stemcell Technologies); 100 ng/ml insulin-like growth factor 1 (IGF-I) (StemCell Technology); 1 mM N-acetyl-L-cysteine (Sigma-Aldrich); 10 μM Y-27632; 1× B-27 50× without vitamin A (ThermoFisher); 1× N-2 100X (ThermoFisher); 500 nM A-83-01 (MedChemExpress); 10 mM nicotinamide (Sigma-Aldrich); 100 units/ml penicillin and 100 μg/ml streptomycin (ThermoFisher); and 2 mmol/l L-glutamine (ThermoFisher). Cultures were maintained in ultra-low attachment plates to promote spheroid formation in a humidified incubator at 37 °C with 21% oxygen and 5% CO_2. For staining and cell treatments (passages 5–10, depending on the cell line), cells were dispersed with TrypLE™ Express and plated in IbiTreat microscopy dishes (Ibidi GmbH, Gräfelfing, Germany) in the presence of FBS-containing medium to promote cell adhesion.

For hypoxic treatments, cells at 70% confluence were either exposed to continued normoxia or placed in a hypoxic incubator (HeraCell 150) that maintained a constant environment (5% CO_2 and 1% O_2 balanced with N_2) for 24 h. Where indicated, cells were incubated with cell-permeable mono-methyl hydrogen succinate (Sigma-Aldrich) at 1 mM for 24 h.

Hela, MCF7 and 786-O cell lines were authenticated by short tandem repeat profiling, and all cell lines were routinely tested for human pathogens and mycoplasma.

Generation of *SDHB* knockdown cells

SDHB knockout cells were generated using the CRISPR–Cas9 technology. Two sgRNA were designed for the lentiCRISPR v2 vector following the Human GeCKOv2 guidelines: 5′-CACCGTCGCCCTCTCCTTGAGG CGC-3′-5′-AAACGCGCCTCAAGGAGAGGGCGAc-3′ and 5′-CACCG GGCCGGCAACCGGCGCCTCA-3′- 5′-AAACTGAGGCGCCGGTTGC CGGCCc-3′. Then, 150 ng of the lentiCRISPR plasmid (RRID: Addgene_52961, Watertown, MA, USA) was cut with Esp3I (Thermo Scientific) and ligated with annealed oligos (0.5 μM) and T4 DNA ligase (New England Biolabs, Ipswich, MA, USA) in the same reaction, which consisted of 10 cycles of 5 min at 37 °C followed by 10 min at 16 °C. The two plasmids harboring sgRNA sequences or empty vectors (as controls) were transfected into 293 T cells in the presence of lentivirus helper plasmids (VSV-G: RRID:Addgene_8454, and PAX2: RRID:Addgene_12260), and the supernatants were collected after 24 h and 48 h of transfection and mixed. The viruses were used to infect cells in culture flasks at 80% confluence, with 4 μg/mL of polybrene. In total, 4 μg/mL puromycin was used for selection. Genome sequencing of the targeted region in *SDHB*-KO cells, confirmed precise editing at the expected locus.

Immunofluorescence and immunohistochemistry

For immunofluorescence, cells were plated in 96-well plates with square bottoms (μ-Plate 96 well square, Ibidi, GmbH, Gräfelfing, Germany) and fixed with 100 μL of 4% paraformaldehyde for 20 min. Primary antibodies were incubated overnight at 4 °C with the primary antibody diluted in 1× PBS containing 1% BSA and 0.3% Triton X-100. The primary antibodies used were: anti-tyrosine hydroxylase antibody (Abcam Cat# ab6211, RRID:AB_2240393), diluted 1:200; anti-synaptophysin (Abcam Cat# ab32127, RRID:AB_2286949, Abcam, Cambridge, UK), diluted 1:250; anti-nestin (Abcam Cat# ab22035, RRID:AB_446723), diluted 1:100; anti-HIF2α (Abcam Cat# ab243861, RRID:AB_3677457), diluted 1:50. For secondary antibody staining, the following antibodies were used: goat anti-rabbit IgG (H + L), highly cross-adsorbed secondary antibody, Alexa Fluor™ Plus 555 (Thermo Fisher Scientific Cat# A32732, RRID:AB_2633281) or goat anti-mouse IgG (H + L), highly cross-adsorbed secondary antibody, Alexa Fluor™ 488 (Thermo Fisher Scientific Cat# A-11029, RRID:AB_2534088). Secondary antibodies were diluted 1:500 and incubated for 2 hours at room temperature, protected from light. To stain the DNA, DAPI solution (Ibidi, GmbH) was added to the cells. Finally, imaging was performed using a Zeiss AxioObserver Z1 microscope (RRID:SCR_021351, Carl Zeiss, Germany). For immunohistochemical analysis of SDHB, FFPE human tumor tissue blocks were cut into 4-μm sections and mounted on poly-L-lysine-coated slides. Antigen retrieval was performed using a high pH EnVision™ FLEX target retrieval solution for 20 min in a Dako PT link platform (Dako Denmark A/S, Glostrup, Denmark), followed by staining with a Dako EnVision™ Flex detection system. Tissue sections were incubated with primary antibody against SDHB (Sigma-Aldrich Cat# HPA002868, RRID:AB_1079889), diluted 1:500. Positive (liver tissue) and negative controls were also included. Samples with complete absence of SDHB immunostaining or with diffuse (not punctate) weak cytoplasmic staining in the presence of positive blood vessel cells and positive inflammatory cells (defined as internal positive controls) were scored as negative. Samples with cytoplasmic punctate staining, irrespective of the intensity, were considered positive. Representative immunohistochemical staining patterns are shown in Supplementary Fig. S1.

Cell proliferation assay

Cells were plated in 96-well plates at 1500 cells per well. After 24 h, once the cells adhered, the medium was removed, and 100 μl of glucose-free DMEM medium (Gibco, ThermoFisher) without supplements was added to each well. When indicated, cells were treated with 12 mM D-(−)-Fructose (Sigma-Aldrich, St. Louis, Missouri, USA) or 1 mM mono-methyl hydrogen succinate (Sigma-Aldrich). Cell proliferation was determined after 72 h using the MTS colorimetric method (Promega Corporation, Madison, WI, USA). In total, 20 μl of MTS reagent was added to each well and incubated for 1 h at 37 °C and 5% CO_2 in darkness. After the incubation, absorbance was measured at a wavelength of 490 nm.

RT-quantitative PCR

RNA extraction was performed using the commercial kit GeneJET RNA Purification Kit (ThermoFisher), following the manufacturer's instructions. cDNA was synthesized using the Maxima First Strand cDNA synthesis kit (ThermoFisher). Quantitative PCR was performed using TaqMan probes for *SLC2A5, SLC2A1, SLC2A8* and *SDHB* (ThermoFisher). Relative expression to peptidylprolyl isomerase A (*PPIA*) (ThermoFisher) target gene was assessed to normalize RNA input amounts and perform relative quantifications.

Western blotting

Cells at 70–80% confluence were lysed using RIPA buffer (Sigma-Aldrich, St. Louis, Missouri, USA). Proteins (30 μg) were fractionated by SDS-PAGE and transferred to PVDF membranes (Bio-Rad Laboratories, CA, USA). Membranes were probed with anti-SDHB antibody (Sigma-Aldrich Cat# HPA002868, RRID:AB_1079889) at 1:1000 dilution. Anti-β-actin (Sigma-Aldrich, Cat# A1978, RRID:AB_476692) was used as a loading control. Bound antibodies were detected with IRDye 800 (Thermo Fisher Scientific Cat# SA5-10172, RRID:AB_2556752) or IRDye 680 IgG (LI-COR Biosciences, Lincoln, NE, USA, Cat# 926-32221, RRID:AB_621841) secondary antibodies (1:10,000, LI-COR Bioscience, Lincoln, NE, USA) and visualized using the Odyssey Fc Imaging System (LI-COR Biosciences, Lincoln, NE, USA). Supplementary Data 3 provides the uncropped western blot source images.

Statistics and reproducibility

Statistical analyses were performed using standard statistical methods as described in the Figure legends. Data are presented as mean ± standard error of the mean (SEM). Statistical significance was determined using appropriate tests depending on data distribution and experimental design, including Student's *t*-test for comparisons between two groups. A p value < 0.05 was considered statistically significant.

All experiments were performed with a minimum of three independent biological replicates, as indicated in the corresponding figure legends. Biological replicates are defined as independent experiments performed on separate days using independently prepared cell cultures. The exact number of biologically independent experiments used for each analysis is provided either in the corresponding Figure legends or in the file "Numerical data for Figures". For experiments where statistical analysis was not applied (e.g., representative images), reproducibility was ensured by repeating experiments independently at least three times with similar results. The numerical source data for graphs in Figs. 5 and 6 are provided in Supplementary Data 4.

Reporting summary

Further information on research design is available in the Nature Portfolio Reporting Summary linked to this article.

Data availability

The DNA methylation data generated in this study have been deposited in the ArrayExpress database under accession number E-MTAB-15178. The source data underlying the Figures are provided in the file "Numerical data for Figures". All other data supporting the findings of this study are available from the corresponding author upon reasonable request.

Received: 9 April 2025; Accepted: 7 January 2026;
Published online: 15 January 2026

References

1. Varghese, J., Skefos, C. M. & Jimenez, C. Metastatic pheochromocytoma and paraganglioma: integrating tumor biology in clinical practice. *Mol. Cell Endocrinol.* **592**, 112344 (2024).
2. Astuti, D. et al. Gene mutations in the succinate dehydrogenase subunit SDHB cause susceptibility to familial pheochromocytoma and to familial paraganglioma. *Am. J. Hum. Genet.* **69**, 49–54 (2001).
3. Bayley, J.-P. et al. SDHAF2 mutations in familial and sporadic paraganglioma and phaeochromocytoma. *Lancet Oncol.* **11**, 366–372 (2010).
4. Burnichon, N. et al. SDHA is a tumor suppressor gene causing paraganglioma. *Hum. Mol. Genet.* **19**, 3011–3020 (2010).
5. Baysal, B. E. et al. Mutations in SDHD, a mitochondrial complex II gene, in hereditary paraganglioma. *Science* **287**, 848–851 (2000).
6. Letouzé, E. et al. SDH mutations establish a hypermethylator phenotype in paraganglioma. *Cancer Cell* **23**, 739–752 (2013).
7. Geli, J. et al. Global and regional CpG methylation in pheochromocytomas and abdominal paragangliomas: association to malignant behavior. *Clin. Cancer Res.* **14**, 2551–2559 (2008).
8. Pollard, P. J. et al. Accumulation of Krebs cycle intermediates and over-expression of HIF1alpha in tumours which result from germline FH and SDH mutations. *Hum. Mol. Genet.* **14**, 2231–2239 (2005).
9. Pollard, P. J. et al. Expression of HIF-1alpha, HIF-2alpha (EPAS1), and their target genes in paraganglioma and pheochromocytoma with VHL and SDH mutations. *J. Clin. Endocrinol. Metab.* **91**, 4593–4598 (2006).
10. Selak, M. A. et al. Succinate links TCA cycle dysfunction to oncogenesis by inhibiting HIF-alpha prolyl hydroxylase. *Cancer Cell* **7**, 77–85 (2005).
11. Cervera, A. M., Bayley, J.-P., Devilee, P. & McCreath, K. J. Inhibition of succinate dehydrogenase dysregulates histone modification in mammalian cells. *Mol. Cancer* **8**, 89 (2009).
12. Xiao, M. et al. Inhibition of α-KG-dependent histone and DNA demethylases by fumarate and succinate that are accumulated in mutations of FH and SDH tumor suppressors. *Genes Dev.* **26**, 1326–1338 (2012).
13. Killian, J. K. et al. Succinate dehydrogenase mutation underlies global epigenomic divergence in gastrointestinal stromal tumor. *Cancer Discov.* **3**, 648–657 (2013).
14. Blank, A. et al. SDHB loss predicts malignancy in pheochromocytomas/sympathethic paragangliomas, but not through hypoxia signalling. *Endocr. Relat. cancer* **17**, 919–928 (2010).
15. Morin, A. et al. TET-mediated hypermethylation primes SDH-deficient cells for HIF2α-driven mesenchymal transition. *Cell Rep.* **30**, 4551–4566.e7 (2020).
16. de Cubas, A. A. et al. DNA methylation profiling in pheochromocytoma and paraganglioma reveals diagnostic and prognostic markers. *Clin. Cancer Res* **21**, 3020–3030 (2015).
17. Taïeb, D. et al. Management of phaeochromocytoma and paraganglioma in patients with germline SDHB pathogenic variants: an international expert consensus statement. *Nat. Rev. Endocrinol.* **20**, 168–184 (2024).
18. Pamporaki, C. et al. Prediction of metastatic pheochromocytoma and paraganglioma: a machine learning modelling study using data from a cross-sectional cohort. *Lancet Digit. Health* **5**, e551–e559 (2023).
19. Chatzikyriakou, P. et al. A comprehensive characterisation of phaeochromocytoma and paraganglioma tumours through histone protein profiling, DNA methylation and transcriptomic analysis genome wide. *Clin. Epigenetics* **15**, 196 (2023).
20. Fishbein, L. et al. Comprehensive molecular characterization of pheochromocytoma and paraganglioma. *Cancer Cell* **31**, 181–193 (2017).
21. Bernardo-Castiñeira, C. et al. Epigenetic deregulation of protocadherin PCDHGC3 in pheochromocytomas/paragangliomas associated with SDHB mutations. *J. Clin. Endocrinol. Metab.* **104**, 5673–5692 (2019).
22. Janin, M., Davalos, V. & Esteller, M. Cancer metastasis under the magnifying glass of epigenetics and epitranscriptomics. *Cancer Metastasis Rev.* **42**, 1071–1112 (2023).
23. McDonald, O. G. et al. Epigenomic reprogramming during pancreatic cancer progression links anabolic glucose metabolism to distant metastasis. *Nat. Genet.* **49**, 367–376 (2017).
24. Arenillas, C. et al. Convergent genetic adaptation in human tumors developed under systemic hypoxia and in populations living at high altitudes. *Cancer Discov.* **15**, 1037–1062 (2025).
25. Senft, D. Fructose takes a detour to feed cancer. *Nat. Rev. Cancer* **25**, 77 (2025).
26. Sukrithan, V., Perez, K., Pandit-Taskar, N. & Jimenez, C. Management of metastatic pheochromocytomas and paragangliomas: when and what. *Curr. Probl. Cancer* **51**, 101116 (2024).
27. Celada, L. et al. Differential HIF2α protein expression in human carotid body and adrenal medulla under physiologic and tumorigenic conditions. *Cancers (Basel)* **14**, 2986 (2022).
28. Nölting, S. et al. Personalized management of pheochromocytoma and paraganglioma. *Endocr. Rev.* **43**, 199–239 (2022).
29. Shao, Y., Wellman, T. L., Lounsbury, K. M. & Zhao, F.-Q. Differential regulation of GLUT1 and GLUT8 expression by hypoxia in mammary epithelial cells. *Am. J. Physiol. Regul. Integr. Comp. Physiol.* **307**, R237–R247 (2014).
30. Kido, T. et al. Glucose transporter 1 is important for the glycolytic metabolism of human endometrial stromal cells in hypoxic environment. *Heliyon* **6**, e03985 (2020).
31. Bharti, H., Han, S., Chang, H.-W. & Reinberg, D. Polycomb repressive complex 2 accessory factors: rheostats for cell fate decision? *Curr. Opin. Genet. Dev.* **84**, 102137 (2024).
32. Batool, A., Jin, C. & Liu, Y.-X. Role of EZH2 in cell lineage determination and relative signaling pathways. *Front. Biosci. (Landmark Ed.)* **24**, 947–960 (2019).
33. Jiang, L., Huang, L. & Jiang, W. H3K27me3-mediated epigenetic regulation in pluripotency maintenance and lineage differentiation. *Cell Insight* **3**, 100180 (2024).
34. Loh, C. H. & Veenstra, G. J. C. The role of polycomb proteins in cell lineage commitment and embryonic development. *Epigenomes* **6**, 23 (2022).
35. Flora, P., Dalal, G., Cohen, I. & Ezhkova, E. Polycomb repressive complex(es) and their role in adult stem cells. *Genes (Basel)* **12**, 1485 (2021).

36. Zhang, T. et al. Dysregulated lipid metabolism blunts the sensitivity of cancer cells to EZH2 inhibitor. *EBioMedicine* **77**, 103872 (2022).
37. Nocito, M. C. et al. A targetable antioxidant defense mechanism to EZH2 inhibitors enhances tumor cell vulnerability to ferroptosis. *Cell Death Dis.* **16**, 291 (2025).
38. Monteagudo, M. et al. MAML3-fusions modulate vascular and immune tumour microenvironment and confer high metastatic risk in pheochromocytoma and paraganglioma. *Best. Pract. Res. Clin. Endocrinol. Metab.* **38**, 101931 (2024).
39. Hadzi-Petrushev, N. et al. GLUT5-overexpression-related tumorigenic implications. *Mol. Med.* **30**, 114 (2024).
40. Weng, Y. et al. SLC2A5 promotes lung adenocarcinoma cell growth and metastasis by enhancing fructose utilization. *Cell Death Discov.* **4**, 38 (2018).
41. Su, C., Li, H. & Gao, W. GLUT5 increases fructose utilization and promotes tumor progression in glioma. *Biochem. Biophys. Res. Commun.* **500**, 462–469 (2018).
42. Zhao, P. et al. SLC2A5 overexpression in childhood philadelphia chromosome-positive acute lymphoblastic leukaemia. *Br. J. Haematol.* **183**, 242–250 (2018).
43. Liang, R. J. et al. GLUT5 (SLC2A5) enables fructose-mediated proliferation independent of ketohexokinase. *Cancer Metab.* **9**, 12 (2021).
44. Shen, Z. et al. GLUT5-KHK axis-mediated fructose metabolism drives proliferation and chemotherapy resistance of colorectal cancer. *Cancer Lett.* **534**, 215617 (2022).
45. Yang, J. et al. Fructose utilization enhanced by GLUT5 promotes lung cancer cell migration via activating glycolysis/AKT pathway. *Clin. Transl. Oncol.* **25**, 1080–1090 (2023).
46. Yu, P.-C. et al. SMARCA5 reprograms AKR1B1-mediated fructose metabolism to control leukemogenesis. *Dev. Cell* **59**, 1954–1971.e7 (2024).
47. Oppelt, S. A., Zhang, W. & Tolan, D. R. Specific regions of the brain are capable of fructose metabolism. *Brain Res.* **1657**, 312–322 (2017).
48. Yan, H. et al. Hexokinase 2 senses fructose in tumor-associated macrophages to promote colorectal cancer growth. *Cell Metab.* **36**, 2449–2467.e6 (2024).
49. Aryee, M. J. et al. Minfi: a flexible and comprehensive bioconductor package for the analysis of infinium DNA methylation microarrays. *Bioinformatics* **30**, 1363–1369 (2014).
50. Triche, T. J., Weisenberger, D. J., Van Den Berg, D., Laird, P. W. & Siegmund, K. D. Low-level processing of illumina infinium DNA methylation BeadArrays. *Nucleic Acids Res.* **41**, e90 (2013).
51. Teschendorff, A. E. et al. A beta-mixture quantile normalization method for correcting probe design bias in Illumina Infinium 450 k DNA methylation data. *Bioinformatics* **29**, 189–196 (2013).
52. Pidsley, R. et al. Critical evaluation of the Illumina MethylationEPIC BeadChip microarray for whole-genome DNA methylation profiling. *Genome Biol.* **17**, 208 (2016).
53. Du, P. et al. Comparison of Beta-value and M-value methods for quantifying methylation levels by microarray analysis. *BMC Bioinforma.* **11**, 587 (2010).
54. Ritchie, M. E. et al. limma powers differential expression analyses for RNA-sequencing and microarray studies. *Nucleic Acids Res.* **43**, e47 (2015).
55. Phipson, B. & Smyth, G. K. Permutation P-values should never be zero: calculating exact P-values when permutations are randomly drawn. *Stat. Appl. Genet. Mol. Biol.* **9**, Article39 (2010).
56. Pedersen, B. S., Schwartz, D. A., Yang, I. V. & Kechris, K. J. Comb-p: software for combining, analyzing, grouping and correcting spatially correlated P-values. *Bioinformatics* **28**, 2986–2988 (2012).
57. Xu, Z., Niu, L., Li, L. & Taylor, J. A. ENmix: a novel background correction method for Illumina HumanMethylation450 BeadChip. *Nucleic Acids Res.* **44**, e20 (2016).
58. Phipson, B., Maksimovic, J. & Oshlack, A. missMethyl: an R package for analyzing data from Illumina's HumanMethylation450 platform. *Bioinformatics* **32**, 286–288 (2016).
59. Subramanian, A. et al. Gene set enrichment analysis: a knowledge-based approach for interpreting genome-wide expression profiles. *Proc. Natl. Acad. Sci. USA* **102**, 15545–15550 (2005).

Acknowledgements

This work was supported by the Instituto de Salud Carlos III (grant number PI20/01754), co-funded by the European Regional Development Fund/ European Social Fund "A way to make Europe"/"Investing in your future") and the MCIN/AEI/10.13039/501100011033 (project PID2023-151388OB-I00 funded by the "European Union NextGenerationEU/PRTR). Tamara Cubiella and Jaime San-Juan-Guardado thank the Consejería de Ciencia, Innovación y Universidad (Principado de Asturias) for Severo-Ochoa pre-doctoral contracts. Alvaro-Suárez-Priede thanks the Spanish Association Against Cancer (AECC) for the predoctoral contract. Nerea Gómez-Suarez thanks the Institute of Oncology of the Principality of Asturias (IUOPA) for the predoctoral contract. We would like to thank the Molecular Histopathology Unit of IUOPA for their invaluable support and contributions to this research.

Author contributions

Conceptualization: M.-D.C., Methodology: T.C., J.-J.A.-L., J.S.-J.-G., and A.S.-P. Formal analysis: M.-D.C., T.C., and JJ.A.-L. Investigation: M.-D.C., T.C., N.G.-S., and JJ.A.-L. Resources: M.T., I.B., C.V., T.S., I.T., M.D.O., L.F., and N.V. Data Analysis: T.C., and JJ.A-L. Writing original draft: M.-D.C. Writing—review and editing: M.-D.C., T.C., M.F.F., and JJ.A.-L. Visualization: M.-D.C., T.C., and JJ.A.-L. Supervision: M.-D.C. Project administration: M.-D.C. Funding acquisition: M.-D.C., T.C., and JJ.A.-L. contributed equally to this work.

Competing interests

The authors declare no competing interests.

Additional information

Supplementary information The online version contains supplementary material available at https://doi.org/10.1038/s42003-026-09543-9.

Correspondence and requests for materials should be addressed to María-Dolores Chiara.

Peer review information *Communications Biology* thanks the anonymous reviewers for their contribution to the peer review of this work. Primary Handling Editors: Christina Karlsson Rosenthal.

Reprints and permissions information is available at http://www.nature.com/reprints

Publisher's note Springer Nature remains neutral with regard to jurisdictional claims in published maps and institutional affiliations.

Open Access This article is licensed under a Creative Commons Attribution-NonCommercial-NoDerivatives 4.0 International License, which permits any non-commercial use, sharing, distribution and reproduction in any medium or format, as long as you give appropriate credit to the original author(s) and the source, provide a link to the Creative Commons licence, and indicate if you modified the licensed material. You do not have permission under this licence to share adapted material derived from this article or parts of it. The images or other third party material in this article are included in the article's Creative Commons licence, unless indicated otherwise in a credit line to the material. If material is not included in the article's Creative Commons licence and your intended use is not permitted by statutory regulation or exceeds the permitted use, you will need to obtain permission directly from the copyright holder. To view a copy of this licence, visit http://creativecommons.org/licenses/by-nc-nd/4.0/.

© The Author(s) 2026

[1]Institute of Oncology of Principality of Asturias, Universidad de Oviedo, Oviedo, Spain. [2]Health Research Institute of Principality of Asturias, Oviedo, Spain. [3]Cancer Epigenetics and Nanomedicine Laboratory, Nanomaterials and Nanotechnology Research Center-Spanish National Research Council (CINN-CSIC), Universidad de Oviedo, Oviedo, Spain. [4]Biomedical Research Networking Center on Rare Diseases (CIBERER), Institute of Health Carlos III, Madrid, Spain. [5]Unidad de Gestión Clínica of Endocrinology and Nutrition, Hospital Virgen Macarena, Seville, Spain. [6]Division of Endocrinology, Diabetes, Metabolism, and Nutrition, Mayo Clinic, Rochester, Minnesota, USA. [7]Service of Endocrinology and Nutrition, Hospital Universitario de Bellvitge, Barcelona, Spain. [8]Service of Pathology, Hospital Universitario de Bellvitge, Barcelona, Spain. [9]Service of Medical Oncology, Hospital Provincial de Castellón, Castellón, Spain. [10]Service of Endocrinology and Nutrition, Hospital Universitario La Fe, Valencia, Spain. [11]Service of Endocrinology and Nutrition, Complejo Universitario de Navarra, Pamplona, Spain. [12]Endocrinology and Nutrition Department, Hospital Universitario Cruces, Biobizkaia, UPV/EHU, CIBERDEM, CIBERER, Endo-ERN, Barakaldo, Bizkaia, Spain. [13]Department of Organisms and Systems Biology (B.O.S.), Universidad of Oviedo, Oviedo, Spain. [14]These authors contributed equally: Tamara Cubiella, Juan José Alba-Linares. ✉e-mail: mdchiara.uo@uniovi.es